CALCIUM SIGNALING

Essential requirement for JPT2 in NAADP-evoked Ca²⁺ signaling

Gihan S. Gunaratne^{1,2}, Eugen Brailoiu³, Shijun He⁴, Ellen M. Unterwald³, Sandip Patel⁵, James T. Slama³*, Timothy F. Walseth¹*, Jonathan S. Marchant²*[†]

Nicotinic acid adenine dinucleotide phosphate (NAADP) is a second messenger that releases Ca²⁺ from acidic organelles through the activation of two-pore channels (TPCs) to regulate endolysosomal trafficking events. NAADP action is mediated by NAADP-binding protein(s) of unknown identity that confer NAADP sensitivity to TPCs. Here, we used a "clickable" NAADP-based photoprobe to isolate human NAADP-binding proteins and identified Jupiter microtubule-associated homolog 2 (JPT2) as a TPC accessory protein required for endogenous NAADP-evoked Ca²⁺ signaling. JPT2 was also required for the translocation of a severe acute respiratory syndrome coronavirus 2 (SARS-CoV-2) pseudovirus through the endolysosomal system. Thus, JPT2 is a component of the NAADP receptor complex that is essential for TPC-dependent Ca²⁺ signaling and control of coronaviral entry.

Copyright © 2021 The Authors, some rights reserved; exclusive licensee American Association for the Advancement of Science. No claim to original U.S.

INTRODUCTION

The second messenger nicotinic acid adenine dinucleotide phosphate (NAADP) releases Ca^{2+} from acidic Ca^{2+} stores within the endolysosomal system (1, 2). NAADP-evoked Ca^{2+} release regulates numerous cellular processes (2, 3), including the trafficking of physiological substrates and pathological cargoes [such as viruses (4–7)] through the endolysosomal system. Dysfunction of this pathway has been implicated in several disease states (8).

Despite the (patho)physiological importance of NAADP-evoked Ca²⁺ signaling, our understanding of the molecular basis for NAADP action remains incomplete. Several ion channel targets for NAADP have been proposed, with the majority of evidence supporting NAADP activation of two-pore channels (TPCs) that reside in endosomes and lysosomes (9, 10). However, no direct binding site for NAADP has been identified on TPCs in over a decade since their first characterization in mammals (11–13). Rather, NAADP is thought to exert its potent Ca²⁺-mobilizing activity by binding to unidentified NAADP-binding accessory protein(s) within the TPC complex (14). In T lymphocytes, NAADP has alternatively been shown to release Ca²⁺ from the endoplasmic reticulum (ER) through the type 1 ryanodine receptor (RyR1) (15). No direct NAADP-binding site has been identified on RyR1.

Direct experimental support for the NAADP-binding protein model derives from photolabeling studies in which NAADP-derivatized photoprobes identify a low-molecular weight NAADP-binding protein (~22/23 kDa) distinct from TPCs and RyRs in various mammalian cells (9, 16–20). The binding characteristics of NAADP to the NAADP-binding protein recapitulate key properties of NAADP-evoked Ca²⁺ release, including a characteristic pharmacology, high affinity, and selectivity for NAADP over nicotinamide

adenine dinucleotide phosphate [NADP; ~11-fold; (16)]. Photolabeling of the NAADP-binding protein, but not NAADP-evoked Ca²⁺ release, persists in TPC knockout models (9, 16), and NAADPbinding proteins are coimmunoprecipitated with TPCs in sea urchin egg homogenates (17). Therefore, the ~23-kDa NAADP-binding protein is a distinct molecular entity from TPCs, the identity of which is unknown. Here, we used a chemical biology and proteomic approach to identify the photolabeled ~23-kDa mammalian NAADP-binding protein as Jupiter microtubule-associated homolog 2 (JPT2) and reveal its essential role in both NAADP-evoked Ca²⁺ signaling and cell entry of severe acute respiratory syndrome coronavirus 2 (SARS-CoV-2) pseudovirus.

RESULTS

Photolabeling of JPT2 by a "clickable" NAADP-derived affinity probe

A bifunctional photoprobe, [³²P]-alkyne-"all-in-one-click" (AIOC)–NAADP, was synthesized and used to profile NAADP-binding proteins in various human cell types. In human erythrocytes, analysis of radiolabeling patterns revealed strong and selective photolabeling of a ~23-kDa NAADP-binding protein (Fig. 1, A and B) compared to other human cell lines (*16*, *18*–*20*). Photolabeling of the ~23-kDa NAADP-binding protein was protected by coincubation with NAADP (Fig. 1, A and B).

Fractionation of erythrocyte whole-cell lysate revealed that the NAADP-binding protein was exclusively found in the soluble ("S20") supernatant (Fig. 1, C and D). Incubation with other nucleotide analogs or other Ca²⁺-mobilizing messengers failed to shield photolabeling of the NAADP-binding protein (Fig. 1, E and F). However, incubation with NAADP, unlabeled alkyne-AIOC-NAADP, or high concentrations of NADP inhibited photolabeling. Characterization of selectivity demonstrated ~11-fold selectivity for NAADP [median inhibitory concentration (IC50) = 80 ± 7 nM] over NADP (IC50 = 871 ± 120 nM; Fig. 1, G and H), in agreement with previous photolabeling data (16). Together, these data authenticate human erythrocytes as an enriched biological source of the ~23-kDa NAADP-binding protein.

Previous efforts to identify this NAADP-binding protein from other mammalian cells has proved challenging, owing to low

¹Department of Pharmacology, University of Minnesota Medical School, 312 Church Street, Minneapolis, MN 55455, USA. ²Department of Cell Biology, Neurobiology and Anatomy, Medical College of Wisconsin, 8701 Watertown Plank Road, Milwaukee, WI 53226, USA. ³Center for Substance Abuse Research, Lewis Katz School of Medicine at Temple University, Philadelphia, PA 19140, USA. ⁴Department of Medicinal and Biological Chemistry, University of Toledo College of Pharmacy and Pharmaceutical Sciences, 3000 Arlington Avenue, Toledo, OH 43614, USA. ⁵Department of Cell and Developmental Biology, University College London, Gower Street, London WC1E 6BT, UK.

^{*}These authors contributed equally as co-senior authors.

[†]Corresponding author. Email: jmarchant@mcw.edu

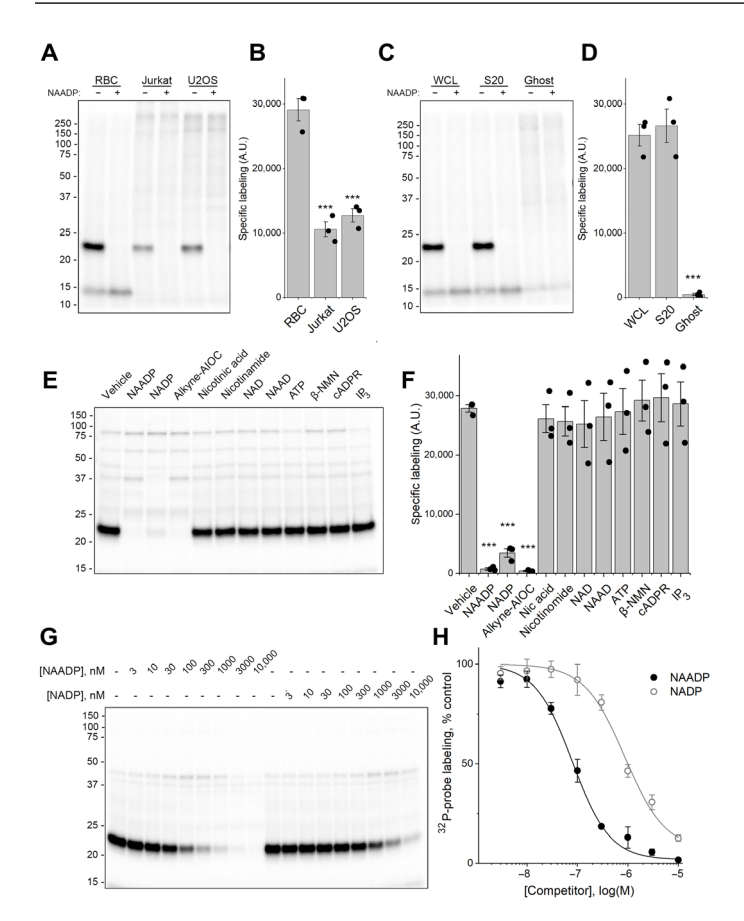


Fig. 1. Characterization of NAADP-binding proteins in human erythrocytes. (**A** and **B**) Red blood cell (RBC), Jurkat, and U2OS whole-cell lysates (WCL) were photolabeled with [32 P]-alkyne-AlOC-NAADP (3 nM) in the absence or presence of competing unlabeled NAADP (10 μM). (**C** and **D**) RBC WCL, S20 cytosol fraction, and "ghost" membrane preparations were photolabeled with [32 P]-alkyne-AlOC-NAADP (3 nM) in the absence or presence of competing unlabeled NAADP (10 μM). (**E** and **F**) RBC S20 was photolabeled with [32 P]-alkyne-AlOC-NAADP (3 nM) in the presence of the indicated compounds (10 μM). (**G** and **H**) RBC S20 was photolabeled with [32 P]-alkyne-AlOC-NAADP (3 nM) in the presence of either NAADP or NADP at the indicated concentration. Data in (B), (D), (F), and (H) represent means ± SD from densitometry analyses of n=3 independent experiments, where representative gels for each specific assay (A, C, E, and G) are shown. Protein (30 μg) was used for all labeling reactions. Data are means ± SEM. Statistical significance was assessed using a univariate regression model (****P<0.005). A.U., arbitrary units.

expression of the endogenous NAADP-binding protein. However, the strong photolabeling of the ~23-kDa NAADP-binding protein in erythrocytes provided better opportunity for a purification effort from the gram quantities of protein available from an easily sourced material (Fig. 2A). In addition, synthesis of a bifunctional probe ([³²P]-alkyne-AIOC-NAADP; Fig. 2B) with both a photoactivatable azide and a clickable alkynyl moiety permitted coupling of photolabeling of the NAADP-binding protein to a subsequent enrichment strategy (Fig. 2A). Proteins were sequentially fractionated using a multistep protocol (fig. S1A). A phosphoprotein enrichment resin was then used to concentrate the NAADP-binding protein using a batch-binding method. When the NAADP-binding protein was not photolabeled, it was retained by the phosphoprotein resin, whereas probe-bound NAADP-binding protein passed through (fig. S1B).

This property was exploited to collect unlabeled eluate after an initial fractionation and elution from the phosphoprotein resin. The unlabeled fraction was then photolabeled with a saturating concentration of alkyne-AIOC-NAADP (which was spiked with a traceable amount of [32P]-alkyne-AIOC-NAADP) to ensure that all NAADP-binding sites were occupied. Probe-bound samples were then incubated with fresh phosphoprotein enrichment resin for a second round of fractionation (Fig. 2, C and D, and fig. S1C). Probe-bound NAADP-binding proteins were biotinylated using a copper-catalyzed azide-alkyne cycloaddition (CuAAC) using "click chemistry" and the biotinylated proteins captured using neutravidin. This protocol resulted in the isolation of a ~23-kDa protein detectable by both silver stain and phosphorimaging (Fig. 2E).

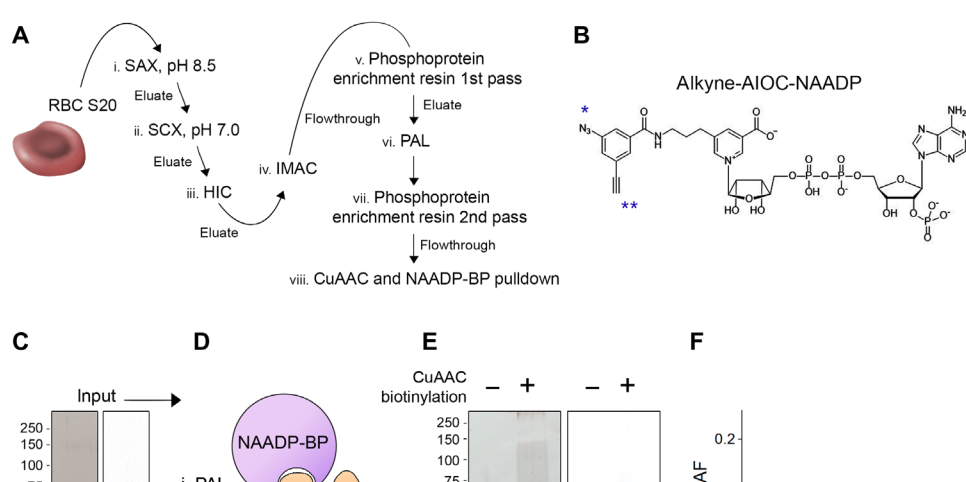
Gel bands from both input control samples and biotin pulldowns were excised and processed for mass spectrometry (MS). Inspection of total spectra revealed JPT2 as the most highly enriched protein (Table 1). Few JPT2 spectra were detected in input control samples, whereas >70-fold enrichment of JPT2 spectra was detected in CuAAC biotin-pulldown samples. No JPT2 spectra were detected in nonbiotinylated CuAAC control samples. Moreover, nearly complete peptide coverage of JPT2 was detected (186 of 190 amino acids). As an alternative ranking measure, total spectral counts from protein hits were processed to yield normalized spectral abundance factor (NSAF) values. Hits were ranked after NSAF values for nonbiotinylated control samples were subtracted from NSAF values for the CuAAC biotin-azide-Plus pulldown samples, which again ranked JPT2 as the top NAADP-binding protein candidate (Fig. 2F). Immunoblotting of erythrocyte chromatography fractions confirmed a progressive enrichment of JPT2 during the serial chromatography procedure (Fig. 2G).

JPT2 properties and expression profile

JPT2 is a short, highly basic protein containing four repeated consensus ("PPGGxxSxxF") sequences, with an additional motif ("MASNIF") characteristic of this gene family located between the first two of these repeats (Fig. 3A) (16). IPT2 mRNA is broadly expressed in human cell lines but is particularly abundant in human cell lines [SKBR3 (7) and U2OS (15)] commonly used to study endogenous NAADP-evoked Ca²⁺ signals (Fig. 3A). In terms of evolutionary pedigree, both members of this conserved gene family (JPT1 and JPT2) are present in numerous vertebrates (21). However, only a single JPT gene is present in basal chordates, echinoderms, and most protostomal phyla (Fig. 3B). Identification of JPT homologs in sea squirts, sea urchins, starfish, and sea slugs is consistent with functional NAADP responses in these organisms (22-25). JPTs are notably absent in the round worm (Caenorhabditis elegans) as are TPCs (Fig. 3B). However, JPT isoforms appear to be absent in platyhelminths despite the presence of TPCs (Fig. 3B). Conversely, a IPT gene is present in fruit flies (Drosophila) in which TPCs are absent (Fig. 3B). Drosophila Jupiter (which has ~27% sequence identity with human JPT2) is a microtubule-associated protein (26), whereas JPT2 is localized to the cell surface, cytoplasm, and nucleus in human cells (21, 27, 28).

Knockdown and pulldown of endogenous JPT2

To validate JPT2 as the photolabeled NAADP-binding protein, we used two independent small interfering RNAs (siRNAs) to knock down endogenous JPT2 in human embryonic kidney (HEK) 293 and U2OS cells. Lysates from siRNA-treated cells were photolabeled,



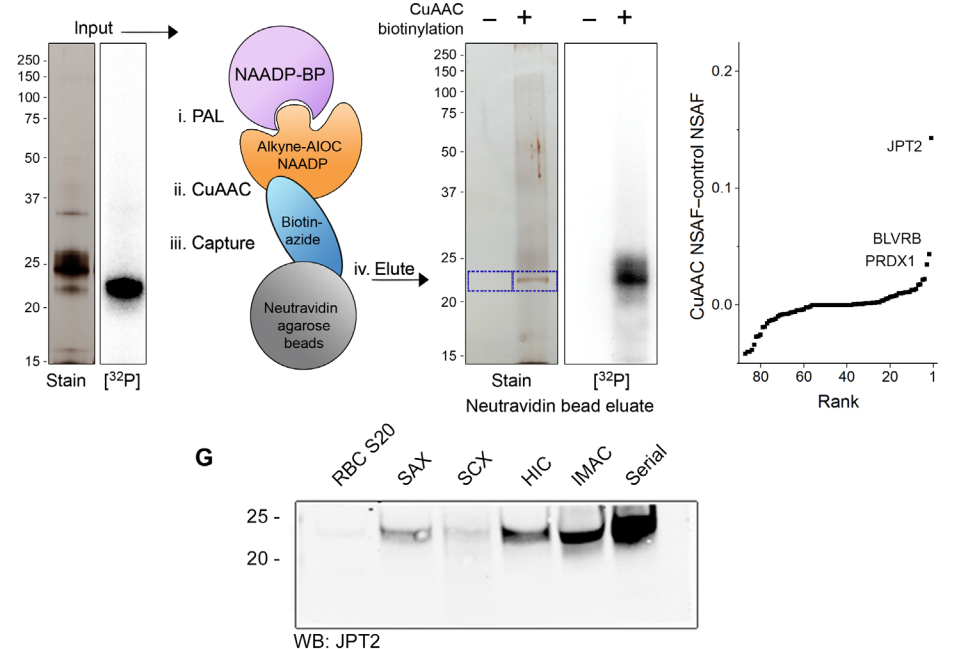


Fig. 2. Biochemical enrichment and isolation of NAADP-binding proteins. (A) Schematic representation of NAADP-binding protein enrichment. RBC S20 proteins were sequentially fractionated in a series of chromatography steps: (i) strong anion exchange (SAX) at pH 8.5, (ii) strong cation exchange (SCX) at pH 7.0, (iii) hydrophobic interaction chromatography (HIC), and (iv) immobilized metal affinity chromatography (IMAC). Eluates from a phosphoprotein enrichment resin were photoaffinity-labeled, and fall-through was collected after passing protein through phosphoprotein enrichment resin a second time (v to vii). (B) Structure of alkyne-AIOC-NAADP. Photolabile aryl azide (*) and clickable alkyne (**) moieties are shown. (C) Silver stain (left) and phosphorimage (right) of 10 μg of sample enriched with NAADP-binding protein. (D) Depiction of approach. NAADP-binding protein is cross-linked to the clickable alkyne-AIOC-NAADP photoprobe, which is biotinylated by copper-catalyzed azide-alkyne cycloaddition (CuAAC). Biotinylated protein is isolated using neutravidin agarose beads. (E) Probe-bound NAADP-binding protein was used in "click" chemistry reaction in the absence or presence of biotin-azide-Plus. Biotinylated protein was captured with neutravidin agarose beads, stringently washed, and eluted. Silver stain (left) and phosphorimage (right) of eluates. Bands of interest are highlighted (blue box). (F) Gel bands of isolated NAADP-binding protein and corresponding bands from input samples and unbiotinylated controls were analyzed by MS. Normalized spectral abundance factor (NSAF) after click and capture minus NSAF of unbiotinylated control samples is shown. (G) Western blot detection of JPT2 in erythrocyte S20 supernatant after fractionation by SAX, SCX, HIC, IMAC, or sequential fractionation through each of these steps (serial).

and the relative intensity of photolabeling patterns was assessed. Cells transfected with either of two *JPT2*-specific siRNAs exhibited reduced photolabeling of the endogenous ~23-kDa NAADP-binding protein (decrease of ~60% in HEK293 and ~50 to 65% in U2OS; Fig. 4, A to D). In contrast, transfection of two nontargeting siRNAs did not reduce photolabeling of the ~23-kDa NAADP-binding protein (Fig. 4, A to D). *JPT2* knockdown was verified by Western

blotting (fig. S2, A and B). JPT2 immunoprecipitated with either of two independent antibodies from erythrocytes (S20) and U2OS cells [S200 lysates (20)] was probed with [32P]-alkyne-AIOC-NAADP. Two different JPT2-specific antibodies, but not an isotyped control immunoglobulin G (IgG) antibody, pulled down the 23-kDa NAADP-binding protein (Fig. 4, E to H). Therefore, both knockdown and immunoprecipitation of endogenous JPT2 validated its identity as the ~23-kDa protein labeled by the NAADP-derived photoprobe.

Recombinant JPT2 selectively binds NAADP

To interrogate whether JPT2 acts as a NAADP-binding protein using an orthogonal approach, we performed [³²P]-NAADP-binding experiments to recombinant human JPT2 isolated from Escherichia coli. Recombinant JPT2 was incubated with [32P]-NAADP in the presence of increasing NAADP or NADP concentrations and binding determined after filtration (Fig. 5A). Densitometry revealed that JPT2 selectively bound NAADP, with displacement of bound [32P]-NAADP being ~17-fold more potent with NAADP (IC₅₀ = $20 \pm$ 3.6 nM) than with NADP (IC₅₀ = 334 \pm 76 nM; Fig. 5B).

JPT2 is a TPC1 accessory protein that regulates responsiveness to NAADP

Does JPT2 interact with TPCs to regulate NAADP-sensitive Ca²⁺ release? First, to assess TPC interactivity, reciprocal immunoprecipitations were performed. In HEK293 cells overexpressing green fluorescent protein (GFP)-tagged TPC constructs, the pulldown of endogenous JPT2 resulted in coimmunoprecipitation of TPC1-GFP but not TPC2-GFP (Fig. 6A). Reciprocally, pulldown of GFP-tagged TPC1, but not TPC2, resulted in coimmunoprecipitation of endogenous JPT2. Second, to assess the impact of JPT2 on endogenous NAADP-evoked Ca²⁺ signals,

Ca²⁺ imaging experiments were performed in single cells directly microinjected with NAADP. In U2OS cells, microinjection of NAADP, but not buffer alone, evoked a rapid Ca²⁺ transient, as shown previously (20). This NAADP-evoked Ca²⁺ signal was similar in cells treated with two unique control siRNAs (Fig. 6, B and C). However, in cells treated with either of the dual siRNAs targeting endogenous JPT2, the amplitude of Ca²⁺ signals caused by NAADP

Table 1. MS dataset. The table depicts the total number of spectral counts (*56*) associated with each identified protein in the indicated experimental samples. Two independent biological replicates were analyzed for each condition (n1, n2). The first two columns present samples before treatment with click chemistry reagents ("input") and without neutravidin-agarose pulldown. The next four columns present samples treated with click reagents either in the absence ("negative control") or presence of hydrazine-cleavable Dde-biotin-picolyl-azide ("Dde-biotin") before neutravidin agarose pulldown and elution with hydrazine treatment. The final four columns present samples treated with click reagents either in the absence (negative control) or presence of biotin-azide-Plus ("Plus-biotin") before neutravidin agarose pulldown and elution with excess free biotin. The table is ranked by total spectral count as the top 20 hits. MW, molecular weight.

	ldentified protein		MW (kDa)	Input		Negative control		Dde-biotin click		Negative control		Plus-biotin click	
				n1	n2	n1	n2	n1	n2	n1	n2	n1	n2
1	Jupiter microtubule- associated homolog 2	JPT2	20	3	7	0	0	231	234	0	0	40	23
2	Hemoglobin subunit alpha	HBA1	15	10	12	11	7	47	61	6	10	30	14
3	Hemoglobin subunit beta	НВВ	16	10	16	6	3	35	41	5	15	26	18
4	Hemoglobin subunit delta	HBD	16	6	14	5	0	30	32	4	11	21	14
5	Junction plakoglobin	JUP	82	8	33	17	7	6	2	14	16	32	0
6	Flavin reductase (NADPH)	BLVRB	22	12	5	0	0	30	9	0	7	24	11
7	Peroxiredoxin-2	PRDX2	22	18	7	3	0	16	8	3	6	10	7
8	Ubiquitin-40S ribosomal protein S27a	RPS27a	18	19	5	0	0	18	4	3	7	9	3
9	Desmoglein-1	DSG1	114	2	13	5	4	0	0	8	9	20	4
10	Filaggrin-2	FLG2	248	7	11	2	0	5	0	8	7	25	0
11	۱-Xylulose reductase	DCXR	26	16	8	0	0	21	8	0	0	7	0
12	Glyceraldehyde- 3-phosphate dehydrogenase	GAPDH	36	5	5	4	0	17	6	3	2	6	2
13	Actin, cytoplasmic 1	ACTB	42	4	2	0	8	5	0	7	7	12	0
14	Peroxiredoxin-1	PRDX1	22	7	5	0	0	10	0	0	0	11	6
15	Serum albumin precursor Isoform 1	ALB	69	6	0	5	4	0	0	7	8	9	0
16	Carbonic anhydrase 1	CA1	29	3	0	2	0	12	4	0	0	6	3
17	Hemoglobin subunit gamma-2	HBG2	16	4	0	0	0	18	0	0	0	6	0
18	Annexin A2	ANXA2	39	2	5	4	2	0	0	3	3	9	0
19	Carbonic anhydrase 2	CA2	29	0	0	3	0	14	4	0	0	5	2
20	Desmocollin-1	DSC1	100	0	3	6	0	0	0	2	5	8	0

microinjection was inhibited (Fig. 6, B and C). The size of NAADP responses in cells treated with siRNA targeting JPT2 was not statistically different from signals evoked by buffer injection (Fig. 6C).

JPT2 regulates coronavirus entry

NAADP-evoked Ca²⁺ release is important for controlling the trafficking of pathogens within the endolysosomal system that are internalized as part of their infective cycle (4–6, 29, 30). For example,

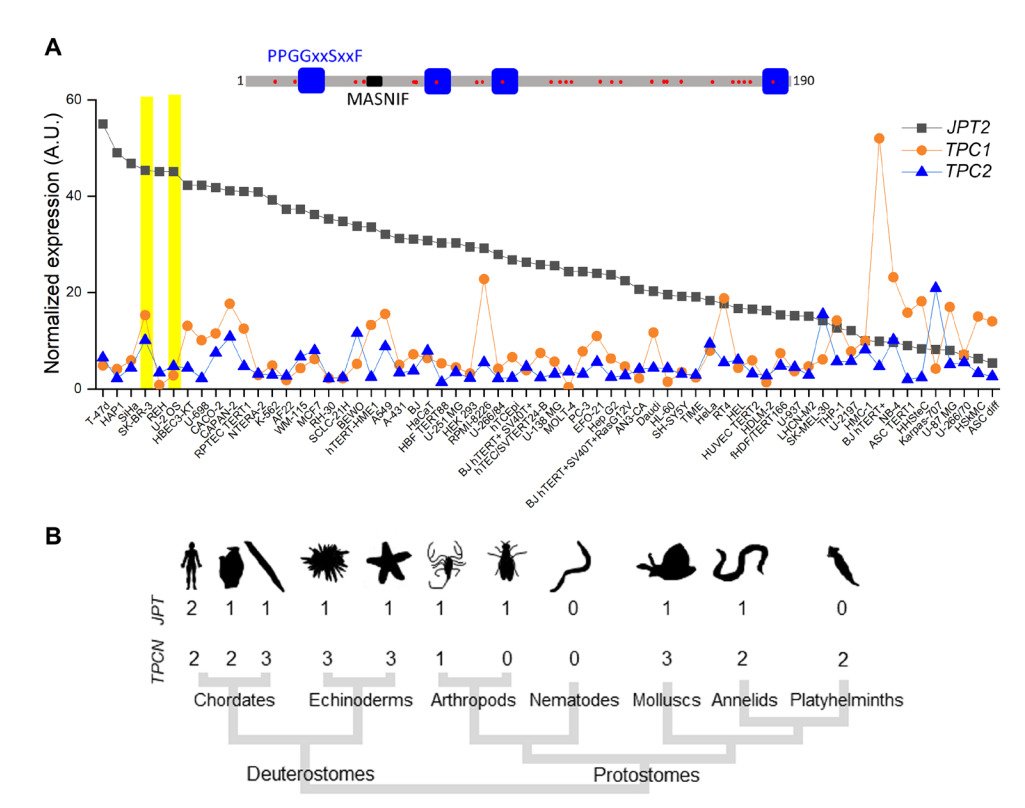


Fig. 3. JPT2 expression profile in cells and organisms. (A) mRNA expression profiling in 64 human cell lines ordered from high to low abundance for JPT2 (black), TPC1 (orange), and TPC2 (blue). SKBR3 and U2OS cells are highlighted (yellow). Data and image credit to The Human Protein Atlas (17): ENSG00000206053-JPT2/cell, available from v19.proteinatlas.org. Inset: Schematic of JPT2 structure to highlight basic residues (circle), four repeat motifs (blue), and the MASNIF motif. (B) Phylogenomic profile of JPT genes. Schematic depicting the number of JPT and TPC homologs in major animal phyla. Organisms, from left to right (accession numbers for JPT): Homo sapiens (NP_653171.1 and NP_001002032.1), Ciona intestinalis (XP_009861954.1), Branchiostoma floridae (XP_002611678.1), Strongylocentrotus purpuratus (XP_011684190.1), Asterias rubens (XP_033631490.1), Centruroides sculpturatus (XP_023222178.1), Drosophila melanogaster (Q917K0), C. elegans, Aplysia californica (XP_005102887.1), Capitella teleta (ELU08900.1), and Schistosoma haematobium.

we have demonstrated that TPCs regulate endolysosomal translocation of a Middle East respiratory syndrome pseudovirus (MERS-CoV) (5, 30). Is JPT2, as an essential component of NAADP-evoked Ca²⁺ responsiveness (Fig. 6, B and C), also required for CoV infectivity? To investigate this issue, we analyzed the role of JPT2 and the TPC complex in the translocation of a SARS-CoV-2 pseudovirus. Viral translocation trafficking was monitored using a reporter assay (5, 30, 31) in which the pseudovirus generates a luminescence signal after release into the cytoplasm, thereby reporting the efficiency of subcellular translocation events [which includes angiotensin converting enzyme 2 (ACE2) receptor binding, internalization, endolysosomal processing and transit, and cytoplasmic release]. First, we tested the effect of the Ca²⁺ chelating agent BAPTA-AM (1,2-bis(2-aminophenoxy) ethane-N,N,N',N'-tetraacetic acid-acetoxymethyl), which resulted in nearly complete inhibition of SARS-CoV-2 pseudovirus infectivity, indicating that intracellular Ca²⁺ signaling plays an essential role for SARS-CoV-2 cellular entry. Next, we analyzed the effects of previously screened inhibitors of NAADP-evoked Ca²⁺ release. Tetrandrine, a TPC blocker (4), which is effective against replication-competent SARS-CoV-2 (32), caused a marked inhibition of SARS-CoV-2 pseudovirus translocation (Fig. 7A). Four

other anti-MERS-CoV compounds that inhibit NAADP-evoked Ca²⁺ release [PF-543, SKF96365, racecadotril, and salmeterol (*30*)] also inhibited cell entry of the SARS-CoV-2 pseudovirus (Fig. 7A). However, drugs targeting inositol 1,4,5-trisphosphate receptors (IP₃Rs) [2-aminoethoxydiphenyl borate (2-APB) and xestospongin] or RyRs (dantrolene and ryanodine) had no effect (Fig. 7B).

Loss-of-function analyses were then performed using siRNAs targeting either JPT1, JPT2, TPCs, or the endolysosomal ion channel TRPML1 (Fig. 7C). Whereas independent control siRNAs or dual siRNAs targeting JPT1 or TRPML1 did not inhibit SARS-CoV-2 pseudovirus translocation, knockdown of endogenous JPT2 markedly inhibited SARS-CoV-2 infectivity, decreasing luminescence to values comparable seen with siRNAs targeting TPCs (Fig. 7B). Inhibition of SARS-CoV-2 was specific to pseudoviral translocation through the acidic Ca²⁺ stores (mediated by spike protein engagement of ACE2), because overexpression of the membrane-anchored protease TMPRSS2 (to cleave the S protein into a fusogenic state at the cell surface) circumvented the observed inhibition (Fig. 7E).

Collectively, these data show that JPT2 is both a NAADP-binding protein (Fig. 5, A and B) and a TPC accessory protein (Fig. 6A). JPT2 function is essential for conferring NAADP sensitivity in human cells, as shown by its

role in NAADP-evoked Ca²⁺ signaling (Fig. 6B) and SARS-CoV-2 cell entry, a NAADP-dependent cellular process (Fig. 7, B and D).

DISCUSSION

Two advances facilitated the unmasking of JPT2 as the ~23-kDa NAADP-binding protein previously identified in human cells (16, 18). The first was the synthesis of a bifunctional probe ([32P]-alkyne-AIOC-NAADP) to selectively photolabel and then enrich NAADP-binding proteins. The second was the serendipitous discovery that human erythrocytes exhibited strong and selective photolabeling of the ~23-kDa NAADP-binding protein. The latter was an unexpected finding given the lack of cytoplasmic organelles and intracellular Ca2+ stores in mature red blood cells (RBCs) (33), although NAADP has been shown to be present (34). The erythrocyte NAADP-binding protein exhibited identical characteristics to the previously characterized mammalian ~23-kDa NAADP-binding protein including a characteristic pharmacology (Fig. 1E) and selectivity for NAADP over NADP (Fig. 1G) (9, 16–20). Consistent with the required properties of a Ca2+ release mechanism that depends on an NAADP-binding protein (14, 35), JPT2

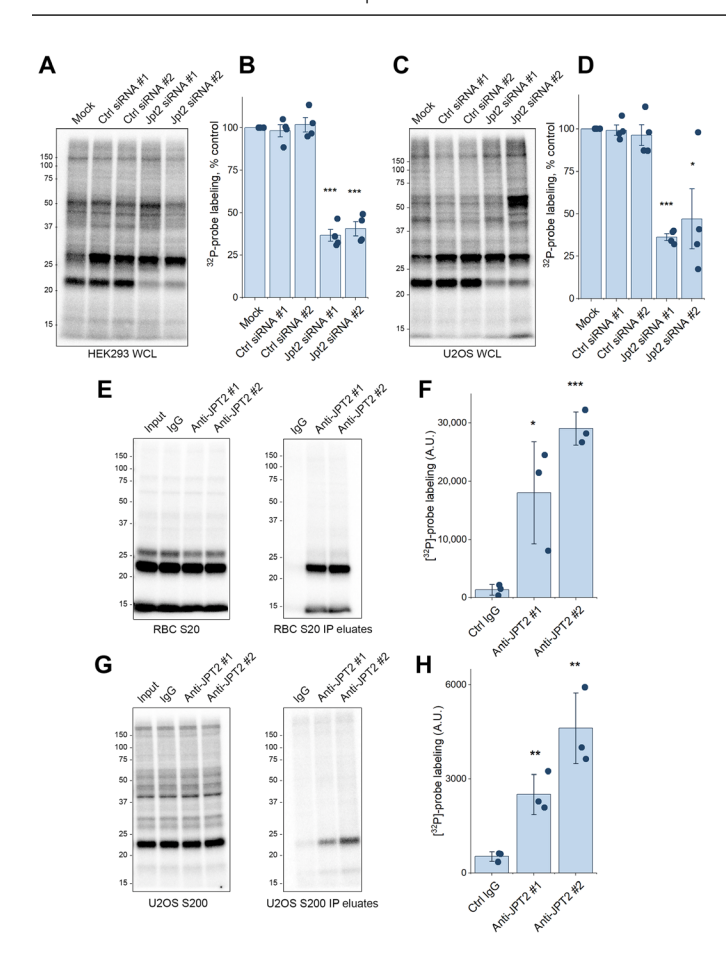


Fig. 4. Photolabeling of NAADP-binding proteins after immunoprecipitation or knockdown of JPT2. (A to D) Knockdown of JPT2 using two nontargeting control siRNAs and two discrete JPT2-specific siRNAs in HEK293 cells (A) and U2OS cells (C). Lysates were photolabeled with $[^{32}P]$ -alkyne-AIOC-NAADP (7 nM). Densitometry analysis (B and D) of samples from n=3 independent knockdown experiments. (E to H) JPT2 was immunoprecipitated from RBC S20 (E) and U2OS S200 (G) using control lgG or two discrete JPT2-specific antibodies. Protein G beads were used to isolate antibody-protein complexes. Left: Ten micrograms of input samples and cleared supernatants after immunoprecipitation were photolabeled with $[^{32}P]$ -alkyne-AIOC-NAADP (7 nM). Right: Immunoprecipitated protein was eluted and photolabeled with $[^{32}P]$ -alkyne-AIOC-NAADP (7 nM). Densitometry analysis (F and H) of photolabeling of immunoprecipitated protein from three independent experiments. Data in (B), (D), (F), and (H) are collected from n=3 independent experiments and shown as means \pm SEM. Statistical significance was assessed using a univariate regression model (*P<0.05, **P<0.01, and ***P<0.005).

binds to NAADP with nanomolar affinity (Fig. 5, A and B), associates with TPC1 (Fig. 6A), and is required for NAADP-evoked Ca²⁺ signals in U2OS cells (Fig. 6, B and C) and NAADP-dependent endolysosomal trafficking processes (Fig. 7, B and D). These data establish JPT2 as an essential component of an NAADP-binding protein complex that confers endogenous NAADP sensitivity to TPCs.

JPT2 [also known as hematological and neurological expressed 1–like (HN1L)] was originally identified in a mouse fertilized egg library (21) and is broadly expressed in human primary tissues and cell lines (Fig. 2G) (11, 19–21, 36). The JPT gene family (JPT1 [HN1] and JPT2 [HN1L]) is also evolutionarily conserved (Fig. 3B) (21), although comparatively little is known about the roles of these

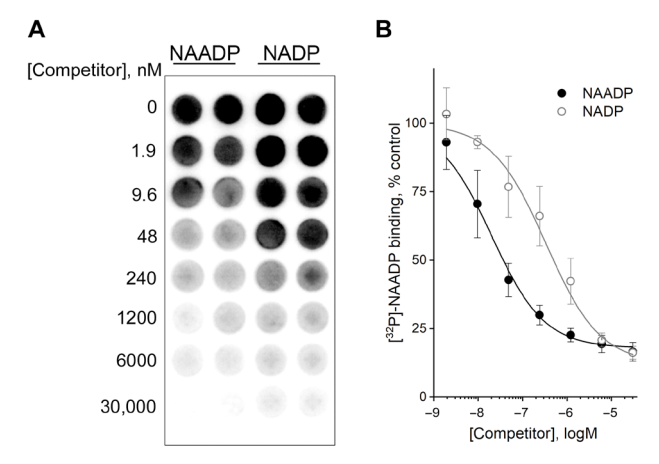


Fig. 5. Recombinant JPT2 binds to NAADP. (**A**) Recombinant JPT2 was incubated with [32 P]-NAADP in the presence of increasing concentrations of unlabeled NAADP or NADP. Representative phosphorimage of multiwell plates used in binding experiments. (**B**) Quantification of bound [32 P]-NAADP in the presence of various concentrations of unlabeled NAADP (closed circle) or NADP (open circle). Data represent mean densitometry [32 P] values \pm SD from n = 3 independent experiments.

family members. JPT2 contains many positively charged residues, which may be relevant for NAADP binding, given the presence of negatively charged pyrophosphate, phosphate, and carboxylate groups in NAADP at physiological pH. Further work will be needed to define this interaction in detail and to investigate the resemblance of the repeat motifs in JPT2 to canonical NA(A)DP-binding sequences (37).

Using T cells, Roggenkamp et al. (38) also identified HN1L/JPT2 as a photolabeled NAADP-binding protein that is critical for the generation of localized Ca²⁺ microdomains observed in the earliest phases of T cell activation (39). These localized Ca²⁺ microdomains appeared to depend on NAADP-dependent activation of RyR1 in the ER (40). Knockdown of HN1L/IPT2 in both human Jurkat cells and rat primary T cells impaired local, and consequently global, Ca²⁺ signals, evoked by T cell receptor and CD3 stimulation (39). Therefore, studies performed in different cell types both converge to implicate JPT2 as a component of NAADP receptor but diverge in their observations that JPT2 confers NAADP sensitivity to different types of intracellular Ca2+ channel: TPCs (this study) or RyRs (38). The hypothesis that NAADP-binding proteins may act to confer NAADP sensitivity to different families of intracellular Ca²⁺ channel, an attractive idea in this field for over a decade (14, 35, 41), receives experimental support from this pair of studies.

Considering the shared pedigree between TPCs and other members of the voltage-gated ion channel family [Ca_v, Na_v, and K_v; (42)], the idea of a multifunctional accessory subunit that binds to NAADP is not unreasonable. The function of each major subfamily of voltage-operated channels is modulated by accessory subunits (14). Many of these accessory protein subunits are promiscuous, with physiological roles dependent on, and independent from, their ion channel partners. Many ion channel accessory proteins have ligand-binding sites, such as FK506 binding proteins (FKBPs), which bind to IP₃Rs and RyRs (43); $\alpha_2\delta$ subunits, which bind to Ca_v (44); nucleotides, which bind to K_{ATP} K⁺ channels (45); and sigma receptors, which bind to Kv1.4 (46). A pertinent example is the Na_v channel β subunit, which is promiscuous and fulfills physiological roles

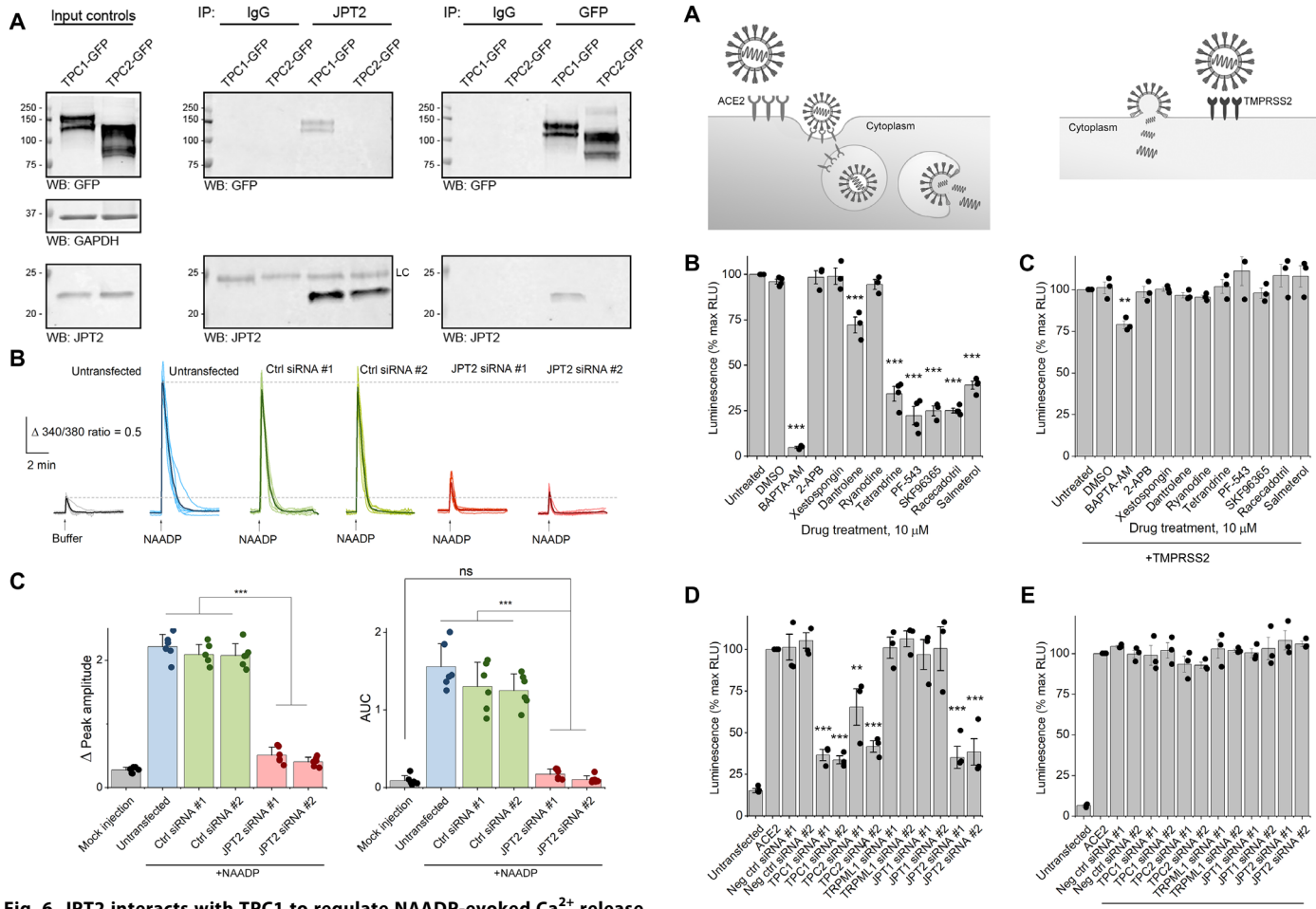


Fig. 6. JPT2 interacts with TPC1 to regulate NAADP-evoked Ca^{2+} release. (A) Coimmunoprecipitation of JPT2 with TPC1. Left: Input controls of lysates from HEK293 cells overexpressing TPC1-GFP or TPC2-GFP. Middle: Endogenous JPT2 immunoprecipitates immunoblotted for GFP to detect TPC1 or TPC2 and JPT2. Right: GFP immunoprecipitates immunoblotted for GFP to detect TPC1 or TPC2 and endogenous JPT2. Data show representative gels from n=3 independent transfections. (B) Traces of intracellular Ca^{2+} flux in response to microinjection of buffer (black) or NAADP (blue, $10 \mu M$ pipette concentration) in individual U2OS cells transfected with two different nontargeting control siRNAs (ctrl siRNA #1 and #2, green) or JPT2-specific siRNAs (siRNA #1 and #2, red). Individual single-cell responses are shown, with the averaged trace bolded. (C) Averaged peak amplitude \pm SD (left) and average area under the curve (AUC; right) are shown from $n \geq 5$ independent cellular injections. P values compared to NAADP injections in untransfected control cells. Data are means \pm SEM. ***P < 0.005. ns, not significant.

independent of the pore-forming subunit in both excitable and non-excitable cells (47). This provides a precedent for JPT2 acting independently from TPCs (in organisms such as *Drosophila* lacking TPCs; Fig. 3B) or TPCs functioning without NAADP activation [acting solely as phosphatidylinositol 3,5-bisphosphate–gated channels (10)]. The ability of JPT2 to associate with both TPC1 and RyR1 is also intriguing in the context of close coupling of these ion channels at tightly apposed membrane contact sites between acidic Ca²⁺ stores and the ER that amplify local NAADP-evoked Ca²⁺ signals into global, whole-cell Ca²⁺ signals (48). The preferential association of JPT2 with TPC1 compared with TPC2 also raises the possibility that multiple NAADP-binding proteins may exist to

Fig. 7. JPT2 regulates SARS-CoV-2 translocation through the endolysosomal system. (A) Schematic to show different routes of SARS-CoV-2 cell entry mediated by ACE2 internalization and translocation through acidic Ca^{2+} stores (left) or fusion at the plasma membrane after spike protein activation by TMPRSS2 (right). (B) Luciferase activity was measured in HEK293 cells transduced with a luciferase-encoding SARS-CoV-2 pseudovirus and expressing ACE2 in the presence of the indicated compound (10 μ M), which inhibit IP₃Rs (2-APB and xestospongin), RyRs (dantrolene and ryanodine), or NAADP-evoked Ca^{2+} release (tetrandrine, PF-543, SKF96365, racecadotril, and salmeterol). (C) Luciferase activity was measured in HEK293 cells transduced with a luciferase-encoding SARS-CoV-2 pseudovirus and expressing TMPRSS2. Cells were treated as in (B). (D and E) Luciferase activity in HEK293 cells transfected with the indicated siRNAs and ACE2 (D) or TMPRSS2 (E), except where indicated (untransfected). Data represent results from n=3 independent assays, with values shown as means \pm SEM. Statistical significance was assessed using a univariate regression model (***P<0.01 and ****P<0.005).

confer NAADP sensitivity and possibly unique functionalities to TPC isoforms. Identification of JPT2 now provides a molecular handle to interrogate these possibilities.

The identification of JPT2 as the photolabeled NAADP-binding protein also implicates a role of NAADP-evoked ${\rm Ca}^{2+}$ signaling in processes for which a functional requirement for JPT2/HN1L has been already established. JPT2 interacts with multiple signaling pathways (49–51), but a consistent theme is a role in cell growth and tumorigenesis. JPT2 overexpression stimulates cell proliferation, tumor growth, and metastasis, whereas JPT2 knockdown

suppresses cell growth and migration (49-51). JPT2 expression is elevated in cancer tissues compared with matched controls, and this up-regulation correlates with poorer patient survival outcomes in several types of cancer (49-52), including non-small cell lung cancer (49,52), hepatocellular carcinoma (50), and triple-negative breast cancer (51). These findings are of special interest, given an emerging focus on NAADP-evoked Ca²⁺ signaling in cancer cell growth (8,53,54).

A second area of pathophysiological relevance, underscored by our data (Fig. 7, B and C), relates to viral infection. JPT2/HN1L inhibits apoptosis in response to viral infection (27). JPT2/HN1L also localizes to Nipah viral particles (a zoonotic paramyxovirus) within host cells (55). Here, we showed that JPT2 supported the endolysosomal translocation but not direct cell surface entry of a SARS-CoV-2 pseudovirus (Fig. 7B), data that extend our previous discovery of a role of the TPC complex in coronaviral infectivity (5, 30). Pharmacological blockade of NAADP-evoked Ca²⁺ release (5, 32) or knockdown of JPT2 (Fig. 7B) impaired the endolysosomal translocation of two different coronaviral spike proteins (MERS and SARS-CoV-2). Given that the endolysosomal processing of SARS-CoV-2 resembles that of MERS-CoV (31), this is expected and provided good rationale to identify ligands that block JPT2 function and NAADP action as broader anti-CoV therapeutics (7). This additional insight into the role of the JPT2/TPC complex in SARS-CoV-2 translocation holds particular importance given the current coronavirus disease 2019 (COVID-19) pandemic, which has infected >100 million people, with more than 2 million fatalities at the time of writing.

In summary, the identification of JPT2 will further our understanding of the mechanism of NAADP action, aiding analysis of how NAADP sensitivity is conferred to TPCs and possibly other intracellular Ca²⁺ channels (14, 35). Resolution of JPT2 as an endogenous mediator of NAADP signaling also opens new opportunities to understand the roles of this understudied gene family in Ca²⁺ signaling processes in both normal physiology and disease states.

MATERIALS AND METHODS

Sample preparation

Human erythrocytes were collected from outdated blood bags supplied by the University of Minnesota Blood Bank Laboratory. Erythrocytes were washed three times in 0.9% saline solution. Packed erythrocytes were then lysed in 3 volumes of hypotonic solution of 10 mM tris-HCl (pH 8.5) supplemented with cOmplete EDTA-free protease inhibitor cocktail (Roche). Erythrocyte lysate was centrifuged at 20,000 relative centrifugal force (RCF) for 30 min, and the supernatant (S20) was reserved for further processing. Protein concentration was determined by Bradford assay (Thermo Fisher Scientific). Jurkat, U2OS, and HEK293 lysates were prepared as previously described (16, 18, 20). Briefly, cells were washed with phosphatebuffered saline (PBS) and collected by centrifugation and scraping. Cell pellets were suspended in 20 mM Hepes (pH 7.4) supplemented with protease inhibitors. Cell suspensions were sonicated to produce whole-cell lysates and subsequently centrifuged at 200,000 RCF. Supernatant (S200) fractions were collected for analysis.

Photoaffinity labeling of NAADP-binding proteins

When determining a scheme for chromatographic enrichment of NAADP-binding proteins, 5 μ g of fractionated protein was incubated with [32 P]-alkyne-AIOC-NAADP at a final concentration of 1

to 7 nM, and reactions were incubated on ice for 1 hour before 2 min of ultraviolet irradiation. When photolabeling protein before click chemistry-based purification, fractionated protein was separately incubated with either alkyne-AIOC-NAADP at a final concentration of 1 µM or incubated with 32P-alkyne-AIOC-NAADP at a final concentration of 5 nM. All reactions were incubated on ice for 1 hour before 2 min of ultraviolet irradiation and mixed again before click chemistry experiments. Photolabeled protein was incubated (<15 min) with SDS sample buffer supplemented with 2-mercaptoethanol (10%). Samples were separated by SDSpolyacrylamide gel electrophoresis (SDS-PAGE) on 12% TGX gels (Bio-Rad). Gels were silver-stained using ProteoSilver (Sigma-Aldrich) and air-dried. The photolabeling was analyzed by exposing the dried gels to MP storage phosphor screens (Packard Instruments). The screens were developed using a Typhoon storage phosphor system. Densitometric analysis was accomplished using ImageJ software.

Chromatographic enrichment of NAADP-binding proteins

Human erythrocyte S20 supernatant was fractionated over various resins as follows. For anion exchange chromatography, a column of Q Sepharose Fast Flow (GE Healthcare) resin was equilibrated with 10 mM Hepes (pH 8.5). Protein samples were pumped onto the column at about 50 mg of protein per milliliter of resin. Retained protein was washed with 3 column volumes of 10 mM Hepes + 50 mM NaCl (pH 8.5). Protein was eluted with 10 mM Hepes + 150 mM NaCl (pH 8.5). For cation exchange chromatography, a column of SP Sepharose Fast Flow (GE Healthcare) resin was equilibrated with 10 mM Hepes (pH 7.0). Protein samples were adjusted to pH 7.0 and pumped onto the column at about 50 mg of protein per milliliter of resin. Retained protein was washed with 3 column volumes of 10 mM Hepes + 30 mM NaCl (pH 7.0). Protein was eluted with 10 mM Hepes + 100 mM NaCl (pH 7.0). For hydrophobic interaction chromatography, Phenyl Sepharose CL-4B (GE Healthcare) resin was equilibrated with 1.5 M (NH₄)₂SO₄ (pH 7.0). Protein samples were supplemented with 1.5 M (NH₄)₂SO₄ and pumped onto the column. Retained protein was washed with 3 column volumes of 1.5 M (NH₄)₂SO₄ (pH 7.0), and protein was eluted in 600 mM (NH₄)₂SO₄ (pH 7.0). For Fe³⁺-nitrilotriacetic acid (NTA) fractionation, Ni2+-NTA resin (Qiagen) was stripped according to vendor protocols and recharged with 0.2 M FeSO₄. Fe³⁺-NTA resin was equilibrated with 300 mM NaCl + 5 mM imidazole and 50 mM Hepes (pH 8.0). Protein samples were diluted 1:10 in equilibration buffer and pumped onto the column, which was washed with 5 volumes of equilibration buffer; flowthrough was collected. For "serial" chromatography, about 8 g of RBC S20 was sequentially fractionated over Q, SP, Phenyl, and NTA resins, in that order. Samples were desalted and concentrated using Amicon Ultra 3-kDa molecular weight cut-off (MWCO) spin filters between each step. The Phosphoprotein Enrichment Kit (Pierce) was used according to vendor protocol for the final stage of enrichment. Protein was incubated with phosphoprotein enrichment resin, and flowthrough and eluates were collected. Samples were desalted and concentrated before photoaffinity labeling as described above. Photolabeled protein samples were then incubated with fresh phosphoprotein enrichment resin for a second time, and flowthrough and eluate fractions were collected.

Click chemistry and capture of NAADP-binding proteins

After sequential chromatographic fractionation and enrichment, protein samples with probe-bound NAADP-binding proteins were

biotinylated using click chemistry. About 250 µg of protein was diluted into 20 mM Hepes (pH 7.4) and supplemented with either 10 μM Dde-biotin-picolyl-azide, 10 μM biotin-azide-Plus, or dimethyl sulfoxide (DMSO). A 40× stock of 60 mM BTTAA (2-[4-((bis[(1tert-butyl-1*H*-1,2,3-triazol-4-yl)methyl]amino)methyl)-1*H*-1,2,3triazol-1-yl|acetic acid) and 12 mM Cu₂SO₄ was prepared in a separate tube. Click reactions were sequentially supplemented with 5 mM aminoguanidine, 1.5 mM BTTAA/300 µM CuSO₄, and 5 mM ascorbic acid, with brief vortexing after each addition. Reactions were incubated for 2 hours at room temperature in an end-over-end mixer. Click reagents were removed by buffer exchange using 3-kDa MWCO ultrafiltration spin columns. Biotinylated protein was captured using 100 μl of neutravidin agarose beads (Thermo Fisher Scientific) at 4°C overnight in an end-over-end mixer. Beads were washed twice with radioimmunoprecipitation assay (RIPA) buffer [50 mM tris base (pH 8.0), 150 mM NaCl, 0.1% SDS, 1% Triton X-100, and 0.5% deoxycholate], twice with PBS + 1% Triton X-100, once with 1 M KCl, twice with 100 mM NaCO₃ (pH 11.5; excluded with Ddebiotin-picolyl azide samples and corresponding controls), twice with 2 M urea, once with RIPA, and three times with PBS. Proteins from CuAAC reactions containing Dde-biotin-picolyl-azide and corresponding controls were eluted by suspending samples in 3% hydrazine + 0.05% SDS and incubating for 30 min at room temperature in an end-over-end mixer. Proteins from CuAAC reactions containing biotin-azide-Plus and corresponding controls were eluted by suspending samples in 10 mM D(+)-biotin + 10 mM EDTA and incubated in a water bath at 90°C for 10 min. Supernatants from both sets of reactions were collected, and elution was repeated two more times. Eluates were concentrated and buffer-exchanged to 20 mM Hepes (pH 7.4) using 3-kDa MWCO spin columns. Eluates were then separated by SDS-PAGE using a 12% Criterion TGX gel and silver-stained. The gels were dried overnight and mounted on a phosphor screen for detection of radiolabeled NAADP-binding proteins. Silver-stained bands that aligned with ³²P signals were excised and analyzed by MS, along with corresponding bands from nonbiotinylated click control samples and input samples.

Mass spectrometry

Proteomic analysis of gel bands was conducted by MS BioWorks (Ann Arbor, MI). In-gel digestion was performed using a ProGest robot (DigiLab) with the following protocol. Samples were washed with 25 mM NH₄HCO₃ and subsequently with acetonitrile, reduced with 10 mM dithiothreitol at 60°C, and alkylated with 50 mM iodoacetamide at room temperature. Samples were digested with trypsin (Promega) at 37°C for 4 hours. Digestions were quenched with formic acid, and supernatants were collected for analysis. Half of each digested sample was analyzed by nano-liquid chromatography-MS/MS (LC-MS/MS) with a Waters M-Class high-performance liquid chromatography (HPLC) system interfaced to a Thermo Fisher Scientific Fusion Lumos mass spectrometer. Peptides were loaded on a trapping column and eluted over a 75-µm analytical column at 350 nl/min; both columns were packed with Luna C18 resin (Phenomenex). The mass spectrometer was operated in data-dependent mode, with the Orbitrap operating at 60,000 and 15,000 full width at half maximum for MS and MS/MS, respectively. The instrument was run with a 3-s cycle for MS and MS/MS. Data were searched using a local copy of Mascot (Matrix Science) with the following parameters: enzyme, trypsin/P; databases, Swiss-Prot Human (concatenated forward and reverse plus common contaminants); fixed

modifications, carbamidomethyl (C); variable modifications, acetyl (N-term), deamidation (N,Q), oxidation (M), and Pyro-Glu (N-term Q); mass values, monoisotopic; peptide mass tolerance, 10 parts per million; fragment mass tolerance, 0.02 Da; max missed cleavages, 2. Mascot DAT files were parsed into Scaffold (Proteome Software) for validation, filtering, and creation of a nonredundant list per sample. Data were filtered using 1% protein and peptide false discovery rate, and at least two unique peptides were required per protein. Relative protein abundance was assessed by calculating NSAF values (56)

$$(NSAF)_{k} = \frac{\left(\frac{SpC}{M_{W}}\right)_{k}}{\sum_{i=1}^{n} \left(\frac{SpC}{M_{W}}\right)}$$

Briefly, total spectral counts (SpC) for an identified protein (k) were normalized to protein size by dividing spectral counts by the predicted mass of the intact protein (M_W), yielding a SAF. Next, SAF values for individual identified proteins were divided by the sum of all SAF values for each identified protein in a given biological sample (n).

Cell culture and transfection

Jurkat cells were maintained in RPMI medium; U2OS and HEK293 cells were maintained in Dulbecco's modified Eagle Medium (DMEM). Cell culture medium was supplemented with 10% fetal bovine serum, penicillin and streptomycin (100 U/ml), and L-glutamine (292 µg/ml), and cells were cultured at 5% CO₂ and 37°C. For plasmid transfection, 3.5×10^5 U2OS or HEK293 cells were seeded in a 35-mm well in the absence of antibiotics. The following day, cells were transfected with siRNA (1 to 20 nM) using RNAiMAX (Thermo Fisher Scientific) according to the vendor's protocol. Medium was changed 24 hours after transfection, and cells were harvested by scraping 48 hours after transfection.

Ca²⁺ imaging

U2OS cells were incubated with fura-2 AM (5 µM; Invitrogen) in Hanks' balanced salt solution (HBSS; room temperature, 45 min in the dark), washed, and incubated for another 45 min to allow for de-esterification. Coverslips were mounted in a custom-designed bath on the stage of an inverted microscope (Nikon Eclipse TE 2000-U, 40× numerical aperture 1.3 oil immersion objective). Cells were superfused (at a flow rate of ~0.5 ml/min) with HBSS, and fluorescence emission (510 nm) was captured with a charge-coupled device camera (Roper Scientific) after alternate excitation at 340 and 380 nm. Captured images were analyzed using MetaFluor software. Single-cell microinjections were performed as previously described (11) using Femtotips II, InjectMan NI 2, and FemtoJet systems (Eppendorf). Pipettes were back-filled with an intracellular solution composed of 110 mM KCl, 10 mM NaCl, and 20 mM Hepes (pH 7.2) and supplemented with NAADP (10 µM). siRNA-transfected cells were selected by identifying cells displaying similar intensities of GFP fluorescence.

Immunoblotting and immunoprecipitation

To immunoprecipitate photolabeled NAADP-binding proteins, erythrocyte S20 and U2OS S200 lysates were incubated with either rabbit IgG isotype control antibody (2 μ g/ml; Thermo Fisher Scientific), anti-HN1L antibody produced in rabbit (0.5 μ g/ml; Sigma-Aldrich,

HPA041908, "anti-JPT2 #1"), or anti-HN1L antibody produced in rabbit (2 µg/ml; Thermo Fisher Scientific, PA5-59774, "anti-JPT2 #2") at 4°C for 1 hour before an overnight incubation with protein G agarose beads (Roche). For coimmunoprecipitation experiments, HEK293 cells overexpressing TPC1-GFP or TPC2-GFP were solubilized in buffer composed of 110 mM KCl, 10 µM CaCl₂, 1% Triton X-100, and 20 mM Hepes (pH7.4) supplemented with Halt phosphatase inhibitor (Pierce) and cOmplete EDTA-free protease inhibitor cocktail (Roche). Lysates were centrifuged at 16,000 RCF for 10 min/4°C, and supernatant was collected. Solubilized lysate (1 mg) was incubated with either rabbit IgG isotype control antibody (2 µg/ml), anti-GFP antibody produced in rabbit (2 µg/ml; Thermo Fisher Scientific, G10362), or anti-HN1L antibody produced in rabbit (2 µg/ml; Sigma-Aldrich, HPA041908) at 4°C for 1 hour before an overnight incubation with protein G agarose beads (Roche). Beads were collected after brief centrifugation and washed three times with PBS + 1% Triton X-100. For photolabeling experiments, immunoprecipitated protein was eluted by rinsing beads three times with 0.2 M glycine (pH 2.6) for 1 min, and rinses were immediately neutralized with 2 M tris base. Immunoprecipitated protein was concentrated and desalted. For coimmunoprecipitation experiments, immunoprecipitated complexes were eluted by incubating beads with 2× Laemmli sample buffer at 95°C for 10 min. For immunodetection of proteins, 20 µg of HEK293 or U2OS wholecell lysate was separated by SDS-PAGE and transferred to nitrocellulose membranes using standard methods. Nitrocellulose membranes were blocked in 5% milk in tris-buffered saline supplemented with 0.1% Tween 20 for 1 hour at room temperature. Membranes were then incubated with primary antibodies at a concentration of 0.05 µg/ml [anti-HN1L, Sigma-Aldrich, HPA041908 and anti-GAPDH (glyceraldehyde-3-phosphate dehydrogenase), Santa Cruz Biotechnology, sc-47724] overnight at 4°C. The following day, membranes were incubated with IRDye secondary antibodies (1:5000 dilution; LI-COR) for 1 hour at room temperature. Signals were detected using a LI-COR Odyssey Imaging system.

Production of recombinant JPT2

Complementary DNA (cDNA) encoding JPT2 (UniProt ID no. Q9H910-3) fused with an N-terminal 6xHis-GST-TEV protease cleavage site was subcloned into pGS-21a bacterial expression vector and transformed into BL21 Star (DE3) *E. coli* cells. A single colony was inoculated into terrific broth (TB) medium and cultured at 37°C. When the OD $_{600}$ (optical density at 600 nm) reached 1.2, the culture was induced with isopropyl- β -D-thiogalactopyranoside at 15°C for 16 hours. Cells were harvested by centrifugation, and cell pellets were resuspended with lysis buffer followed by sonication. Protein was loaded onto a Ni-NTA column, and 6xHis-GST-TEV-JPT2 was eluted with 400 mM imidazole. Protein was treated with TEV protease to remove N-terminal tags, and untagged JPT2 was collected by loading onto a Ni-NTA column and eluting with 10 mM imidazole; samples were concentrated, and buffer was exchanged using 20 mM Hepes (pH 7.4) and 3-kDa MWCO ultrafiltration spin columns.

³²P-NAADP-binding assays

Recombinant JPT2 (20 µg) was incubated with [³²P]-NAADP (~0.33 nM) in the presence of increasing concentrations of cold NAADP or NADP for 1 hour on ice. During the incubation, MultiScreen-IP 96-well polyvinylidene difluoride (PVDF) plates (Millipore) were mounted on a vacuum manifold. PVDF membranes

were wetted with ethanol, followed by two washes with 20 mM Hepes (pH 7.4). Binding reactions were transferred to 96-well PVDF plates and filtered through PVDF membranes. Membranes were washed three times with ice-cold 20 mM Hepes (pH 7.4). Rubber gaskets were removed from the underside of 96-well PVDF plates, and PVDF wells were dried with paper towels. PVDF plates were then placed on phosphor screens and subsequently processed using a Typhoon phosphor storage system. Bound [³²P]-NAADP was quantified by densitometry using ImageJ.

SARS-CoV-2 pseudovirus translocation assays

Cell infection assays were carried out as described previously for MERS-CoV (5, 57). Spike-pseudotyped retroviruses expressing a luciferase reporter gene were prepared by cotransfecting HEK293T cells with a plasmid carrying Env-defective, luciferase-expressing HIV-1 genome (pNL4-3.luc.RE) and a plasmid encoding SARS-CoV-2 spike (S) protein, which is necessary and sufficient to facilitate cell entry. SARS-CoV-2 pseudovirus particles were harvested from supernatant 72 hours after transfection. HEK293 cells (overexpressing ACE2) were used to monitor SARS-CoV-2 pseudovirus translocation. Cells were seeded into 96-well plates (Midwest Scientific) at a concentration of 1×10^4 cells per well. The following day, cells were preincubated with individual drugs (final concentration, 10 µM) for 1 hour before pseudovirus addition. Cells were incubated (5% CO₂/37°C) for an additional 5 hours in the presence of drug and pseudovirus. After 6 hours, the culture medium was replaced with complete DMEM and cells were incubated for a further 60 hours. Cells were then washed three times with Dulbecco's phosphate-buffered saline (ThermoFisher Scientific) and assayed for luciferase activity. Cells were lysed in 80 µl of lysis buffer (Promega) per well, and 40 µl of lysate was transferred to solid-white 96-well plates (Corning) and mixed with 40 µl of luciferase substrate (Promega). Luminescence [relative luminescence units (RLUs)] was measured using a Tecan Infinite M100 microplate reader. Luminescence values are reported relative to values measured in cells treated with virus alone, background-corrected by luminescence values in cells unexposed to virus, except where indicated.

Statistical analysis

A univariate regression model with type as a categorical covariate was used to evaluate differences in intensity between types of samples. Type was coded as a categorical variable with the reference category being the control state or appropriate group against which others were being compared. The coefficients calculated from this regression model were used to calculate the P statistic (*P < 0.05, **P < 0.01, and ***P < 0.005).

Chemicals and molecular reagents

NAADP was synthesized by incubating NADP (Sigma-Aldrich) with nicotinic acid in the presence of recombinant *Aplysia* adenosine 5′-diphosphate–ribosyl cyclase (*58*) and purified by HPLC. The bifunctional probe (alkyne-AIOC-NAADP; fig. S3) was synthesized as described in Supplementary Materials and Methods. NADP was freshly purified by HPLC before experimentation to remove contaminating NAADP (*17*). Nicotinic acid, nicotinamide, nicotinamide adenine dinucleotide, nicotinic acid adenine dinucleotide sodium salt, adenosine 5′-triphosphate disodium salt hydrate, β-nicotinamide ribose monophosphate, and D(+)-biotin were purchased from Sigma-Aldrich. BTTAA, Dde-biotin-picolyl-azide,

and biotin-azide-Plus were purchased from Click Chemistry Tools (Scottsdale, AZ). Silencer Select siRNAs targeted against JPT2 and nontargeting negative control siRNAs were purchased from Thermo Fisher Scientific. siRNA sequences were as follows: JPT2 siRNA #1, GAACCAAAAUCGGAUCUUAtt and JPT2 siRNA #2, CCAAGGAUCAUGUUUUCUUtt.

SUPPLEMENTARY MATERIALS

stke.sciencemag.org/cgi/content/full/14/675/eabd5605/DC1 Materials and Methods

Fig. S1. Chromatographic enrichment of NAADP-binding proteins.

Fig. S2. Validation of knockdown methods.

Fig. S3. Synthesis of alkyne-AIOC-NAADP.

References (59-61)

View/request a protocol for this paper from Bio-protocol.

REFERENCES AND NOTES

- S. Patel, L. Ramakrishnan, T. Rahman, A. Hamdoun, J. S. Marchant, C. W. Taylor, E. Brailoiu, The endo-lysosomal system as an NAADP-sensitive acidic Ca²⁺ store: Role for the twopore channels. *Cell Calcium* 50, 157–167 (2011).
- H. C. Lee, Cyclic ADP-ribose and nicotinic acid adenine dinucleotide phosphate (NAADP) as messengers for calcium mobilization. J. Biol. Chem. 287, 31633–31640 (2012)
- A. Galione, A primer of NAADP-mediated Ca²⁺ signalling: From sea urchin eggs to mammalian cells. Cell Calcium 58, 27–47 (2015).
- Y. Sakurai, A. A. Kolokoltsov, C. C. Chen, M. W. Tidwell, W. E. Bauta, N. Klugbauer, C. Grimm, C. Wahl-Schott, M. Biel, R. A. Davey, Ebola virus. Two-pore channels control Ebola virus host cell entry and are drug targets for disease treatment. *Science* 347, 995–998 (2015)
- G. S. Gunaratne, Y. Yang, F. Li, T. F. Walseth, J. S. Marchant, NAADP-dependent Ca²⁺ signaling regulates Middle East respiratory syndrome-coronavirus pseudovirus translocation through the endolysosomal system. *Cell Calcium* 75, 30–41 (2018).
- N. Khan, P. W. Halcrow, K. L. Lakpa, Z. Afghah, N. M. Miller, S. F. Dowdy, J. D. Geiger, X. Chen, Two-pore channels regulate Tat endolysosome escape and Tat-mediated HIV-1 LTR transactivation. FASEB J. 34, 4147–4162 (2020).
- C. Grimm, R. Tang, Could an endo-lysosomal ion channel be the Achilles heel of SARS-CoV2? Cell Calcium 88, 102212 (2020).
- S. Patel, B. S. Kilpatrick, Two-pore channels and disease. Biochim. Biophys. Acta Mol. Cell Res. 1865, 1678–1686 (2018).
- M. Ruas, L. C. Davis, C. C. Chen, A. J. Morgan, K. T. Chuang, T. F. Walseth, C. Grimm, C. Garnham, T. Powell, N. Platt, F. M. Platt, M. Biel, C. Wahl-Schott, J. Parrington, A. Galione, Expression of Ca²⁺-permeable two-pore channels rescues NAADP signalling in TPC-deficient cells. *EMBO J.* 34, 1743–1758 (2015).
- S. Gerndt, C.-C. Chen, Y.-K. Chao, Y. Yuan, S. Burgstaller, A. S. Rosato, E. Krogsaeter, N. Urban, K. Jacob, O. N. P. Nguyen, M. T. Miller, M. Keller, A. M. Vollmar, T. Gudermann, S. Zierler, J. Schredelseker, M. Schaefer, M. Biel, R. Malli, C. Wahl-Schott, F. Bracher, S. Patel, C. Grimm, Agonist-mediated switching of ion selectivity in TPC2 differentially promotes lysosomal function. *eLife* 9, e54712 (2020).
- E. Brailoiu, D. Churamani, X. Cai, M. G. Schrlau, G. C. Brailoiu, X. Gao, R. Hooper, M. J. Boulware, N. J. Dun, J. S. Marchant, S. Patel, Essential requirement for two-pore channel 1 in NAADP-mediated calcium signaling. J. Cell Biol. 186, 201–209 (2009).
- P. J. Calcraft, M. Ruas, Z. Pan, X. Cheng, A. Arredouani, X. Hao, J. Tang, K. Rietdorf, L. Teboul, K. T. Chuang, P. Lin, R. Xiao, C. Wang, Y. Zhu, Y. Lin, C. N. Wyatt, J. Parrington, J. Ma, A. M. Evans, A. Galione, M. X. Zhu, NAADP mobilizes calcium from acidic organelles through two-pore channels. *Nature* 459, 596–600 (2009).
- X. Zong, M. Schieder, H. Cuny, S. Fenske, C. Gruner, K. Rotzer, O. Griesbeck, H. Harz, M. Biel, C. Wahl-Schott, The two-pore channel TPCN2 mediates NAADP-dependent Ca²⁺-release from lysosomal stores. *Pflugers Arch.* 458, 891–899 (2009).
- J. S. Marchant, Y. Lin-Moshier, T. F. Walseth, S. Patel, The molecular basis for Ca²⁺ signalling by NAADP: Two-pore channels in a complex? *Messenger (Los Angel.)* 1, 63–76 (2012).
- I. M. A. Wolf, B.-P. Diercks, E. Gattkowski, F. Czarniak, J. Kempski, R. Werner, D. Schetelig, H.-W. Mittrücker, V. Schumacher, M. von Osten, D. Lodygin, A. Flügel, R. Fliegert, A. H. Guse, Frontrunners of T cell activation: Initial, localized Ca²⁺ signals mediated by NAADP and the type 1 ryanodine receptor. Sci. Signal. 8, ra102 (2015).
- Y. Lin-Moshier, T. F. Walseth, D. Churamani, S. M. Davidson, J. T. Slama, R. Hooper, E. Brailoiu, S. Patel, J. S. Marchant, Photoaffinity labeling of nicotinic acid adenine dinucleotide phosphate (NAADP) targets in mammalian cells. *J. Biol. Chem.* 287, 2296–2307 (2012).

- T. F. Walseth, Y. Lin-Moshier, P. Jain, M. Ruas, J. Parrington, A. Galione, J. S. Marchant, J. T. Slama, Photoaffinity labeling of high affinity nicotinic acid adenine dinucleotide phosphate (NAADP)-binding proteins in sea urchin egg. J. Biol. Chem. 287, 2308–2315 (2012).
- T. F. Walseth, Y. Lin-Moshier, K. Weber, J. S. Marchant, J. T. Slama, A. H. Guse, Nicotinic acid adenine dinucleotide 2'-phosphate (NAADP) binding proteins in T-lymphocytes. *Messenger (Los Angel.)* 1, 86–94 (2012).
- T. Y. Asfaha, G. S. Gunaratne, M. E. Johns, J. S. Marchant, T. F. Walseth, J. T. Slama, The synthesis and characterization of a clickable-photoactive NAADP analog active in human cells. *Cell Calcium* 83, 102060 (2019).
- G. S. Gunaratne, P. Su, J. S. Marchant, J. T. Slama, T. F. Walseth, 5-Azido-8-ethynyl-NAADP: A bifunctional, clickable photoaffinity probe for the identification of NAADP receptors. *Biochim. Biophys. Acta Mol. Cell Res.* 1866, 1180–1188 (2019).
- G. Zhou, J. Wang, Y. Zhang, C. Zhong, J. Ni, L. Wang, J. Guo, K. Zhang, L. Yu, S. Zhao, Cloning, expression and subcellular localization of HN1 and HN1L genes, as well as characterization of their orthologs, defining an evolutionarily conserved gene family. *Gene* 331, 115–123 (2004).
- H. C. Lee, R. Aarhus, A derivative of NADP mobilizes calcium stores insensitive to inositol trisphosphate and cyclic ADP-ribose. J. Biol. Chem. 270, 2152–2157 (1995).
- M. Albrieux, H. C. Lee, M. Villaz, Calcium signaling by cyclic ADP-ribose, NAADP, and inositol trisphosphate are involved in distinct functions in ascidian oocytes. *J. Biol. Chem.* 273, 14566–14574 (1998).
- L. Santella, K. Kyozuka, A. A. Genazzani, L. De Riso, E. Carafoli, Nicotinic acid adenine dinucleotide phosphate-induced Ca²⁺ release. Interactions among distinct Ca²⁺ mobilizing mechanisms in starfish oocytes. *J. Biol. Chem.* 275, 8301–8306 (2000).
- S. Bezin, G. Charpentier, H. C. Lee, G. Baux, P. Fossier, J. M. Cancela, Regulation of nuclear Ca²⁺ signaling by translocation of the Ca²⁺ messenger synthesizing enzyme ADP-ribosyl cyclase during neuronal depolarization. *J. Biol. Chem.* 283, 27859–27870 (2008).
- N. Karpova, Y. Bobinnec, S. Fouix, P. Huitorel, A. Debec, Jupiter, a new Drosophila protein associated with microtubules. *Cell Motil. Cytoskeleton* 63, 301–312 (2006).
- J. Lei, D. Hu, S. Xue, F. Mao, E. Obeng, Y. Quan, W. Yu, HN1L is essential for cell growth and survival during nucleopolyhedrovirus infection in silkworm, Bombyx mori. *PLOS ONE* 14. e0216719 (2019).
- Z.-B. Liu, N. E. Ezzedine, A. K. Eterovic, J. E. Ensor, H. J. Huang, J. Albanell, D. S. Choi, A. Lluch, Y. Liu, F. Rojo, H. Wong, E. Martínez-Dueñas, Á. Guerrero-Zotano, Z.-M. Shao, J. G. Darcourt, G. B. Mills, B. Dave, J. C. Chang, Detection of breast cancer stem cell gene mutations in circulating free DNA during the evolution of metastases. *Breast Cancer Res. Treat.* 178, 251–261 (2019).
- C. J. Penny, K. Vassileva, A. Jha, Y. Yuan, X. Chee, E. Yates, M. Mazzon, B. S. Kilpatrick,
 Muallem, M. Marsh, T. Rahman, S. Patel, Mining of Ebola virus entry inhibitors identifies approved drugs as two-pore channel pore blockers. *Biochim. Biophys. Acta Mol. Cell Res.* 1866, 1151–1161 (2019).
- G. S. Gunaratne, M. E. Johns, H. M. Hintz, T. F. Walseth, J. S. Marchant, A screening campaign in sea urchin egg homogenate as a platform for discovering modulators of NAADP-dependent Ca²⁺ signaling in human cells. *Cell Calcium* 75, 42–52 (2018).
- J. Shang, Y. Wan, C. Luo, G. Ye, Q. Geng, A. Auerbach, F. Li, Cell entry mechanisms of SARS-CoV-2. Proc. Natl. Acad. Sci. U.S.A. 117, 11727–11734 (2020).
- X. Ou, Y. Liu, X. Lei, P. Li, D. Mi, L. Ren, L. Guo, R. Guo, T. Chen, J. Hu, Z. Xiang, Z. Mu, X. Chen, J. Chen, K. Hu, Q. Jin, J. Wang, Z. Qian, Characterization of spike glycoprotein of SARS-CoV-2 on virus entry and its immune cross-reactivity with SARS-CoV. *Nat. Commun.* 11, 1620 (2020).
- M. Moras, S. D. Lefevre, M. A. Ostuni, From erythroblasts to mature red blood cells: Organelle clearance in mammals. Front. Physiol. 8, 1076 (2017).
- D. Churamani, E. A. Carrey, G. D. Dickinson, S. Patel, Determination of cellular nicotinic acid-adenine dinucleotide phosphate (NAADP) levels. *Biochem. J.* 380, 449–454 (2004).
- A. H. Guse, Linking NAADP to ion channel activity: A unifying hypothesis. Sci. Signal. 5, pe18 (2012).
- M. Uhlen, C. Zhang, S. Lee, E. Sjostedt, L. Fagerberg, G. Bidkhori, R. Benfeitas, M. Arif, Z. Liu, F. Edfors, K. Sanli, K. von Feilitzen, P. Oksvold, E. Lundberg, S. Hober, P. Nilsson, J. Mattsson, J. M. Schwenk, H. Brunnstrom, B. Glimelius, T. Sjoblom, P. H. Edqvist, D. Djureinovic, P. Micke, C. Lindskog, A. Mardinoglu, F. Ponten, A pathology atlas of the human cancer transcriptome. *Science* 357, eaan2507 (2017).
- Y. H. Hua, C. Y. Wu, K. Sargsyan, C. Lim, Sequence-motif detection of NAD(P)-binding proteins: Discovery of a unique antibacterial drug target. Sci. Rep. 4, 6471 (2014).
- H. G. Roggenkamp, I. Khansahib, L. C. Herdnandez, Y. Zhang, D. Lodygin, A. Krüger, F. Gu, F. Mockl, A. Löhndorf, V. Wolters, D. Woike, A. Rosche, A. Bauche, D. Schetelig, R. Werner, H. Schlüter, A. V. Failla, R. Fliegert, C. Meier, T. F. Walseth, A. Flügel, B.-P. Diercks, A. H. Guse, HN1L/JPT2: A signaling protein that connects NAADP generation to Ca²⁺ microdomain formation. Sci. Signal. 14, eabd5647 (2021).
- B. P. Diercks, R. Werner, P. Weidemuller, F. Czarniak, L. Hernandez, C. Lehmann, A. Rosche,
 A. Kruger, U. Kaufmann, M. Vaeth, A. V. Failla, B. Zobiak, F. I. Kandil, D. Schetelig,

SCIENCE SIGNALING | RESEARCH ARTICLE

- A. Ruthenbeck, C. Meier, D. Lodygin, A. Flugel, D. Ren, I. M. A. Wolf, S. Feske, A. H. Guse, ORAl1, STIM1/2, and RYR1 shape subsecond Ca²⁺ microdomains upon T cell activation. *Sci. Signal.* **11**, eaat0358 (2018).
- W. Dammermann, B. Zhang, M. Nebel, C. Cordiglieri, F. Odoardi, T. Kirchberger, N. Kawakami, J. Dowden, F. Schmid, K. Dornmair, M. Hohenegger, A. Flügel, A. H. Guse, B. V. L. Potter, NAADP-mediated Ca²⁺ signaling via type 1 ryanodine receptor in T cells revealed by a synthetic NAADP antagonist. *Proc. Natl. Acad. Sci. U.S.A.* 106, 10678–10683 (2009).
- J. V. Gerasimenko, Y. Maruyama, K. Yano, N. J. Dolman, A. V. Tepikin, O. H. Petersen, O. V. Gerasimenko, NAADP mobilizes Ca²⁺ from a thapsigargin-sensitive store in the nuclear envelope by activating ryanodine receptors. *J. Cell Biol.* 163, 271–282 (2003).
- T. Rahman, X. Cai, G. C. Brailoiu, M. E. Abood, E. Brailoiu, S. Patel, Two-pore channels provide insight into the evolution of voltage-gated Ca²⁺ and Na⁺ channels. Sci. Signal. 7, ra109 (2014).
- T. Vervliet, J. B. Parys, G. Bultynck, Bcl-2 and FKBP12 bind to IP3 and ryanodine receptors at overlapping sites: The complexity of protein-protein interactions for channel regulation. *Biochem. Soc. Trans.* 43, 396–404 (2015).
- C. Eroglu, N. J. Allen, M. W. Susman, N. A. O'Rourke, C. Y. Park, E. Ozkan, C. Chakraborty, S. B. Mulinyawe, D. S. Annis, A. D. Huberman, E. M. Green, J. Lawler, R. Dolmetsch, K. C. Garcia, S. J. Smith, Z. D. Luo, A. Rosenthal, D. F. Mosher, B. A. Barres, Gabapentin receptor α2δ-1 is a neuronal thrombospondin receptor responsible for excitatory CNS synaptogenesis. Cell 139, 380–392 (2009).
- G. M. Martin, M. W. Sung, Z. Yang, L. M. Innes, B. Kandasamy, L. L. David, C. Yoshioka, S.-L. Shyng, Mechanism of pharmacochaperoning in a mammalian K_{ATP} channel revealed by cryo-EM. *eLife* 8, e46417 (2019).
- 46. E. Aydar, C. P. Palmer, V. A. Klyachko, M. B. Jackson, The sigma receptor as a ligand-regulated auxiliary potassium channel subunit. *Neuron* **34**, 399–410 (2002).
- 47. H. A. O'Malley, L. L. Isom, Sodium channel β subunits: Emerging targets in channel opathies. *Annu. Rev. Physiol.* **77**, 481–504 (2015).
- C. J. Penny, B. S. Kilpatrick, E. R. Eden, S. Patel, Coupling acidic organelles with the ER through Ca²⁺ microdomains at membrane contact sites. *Cell Calcium* 58, 387–396 (2015).
- L. Li, T. T. Zeng, B. Z. Zhang, Y. Li, Y. H. Zhu, X. Y. Guan, Overexpression of HN1L promotes cell malignant proliferation in non-small cell lung cancer. *Cancer Biol. Ther.* 18, 904–915 (2017)
- L. Li, Y.-L. Zheng, C. Jiang, S. Fang, T.-T. Zeng, Y. H. Zhu, Y. Li, D. Xie, X.-Y. Guan, HN1L-mediated transcriptional axis AP-2γ/METTL13/TCF3-ZEB1 drives tumor growth and metastasis in hepatocellular carcinoma. *Cell Death Differ.* 26, 2268–2283 (2019).
- Y. Liu, D. S. Choi, J. Sheng, J. E. Ensor, D. H. Liang, C. Rodriguez-Aguayo, A. Polley, S. Benz,
 O. Elemento, A. Verma, Y. Cong, H. Wong, W. Qian, Z. Li, S. Granados-Principal,
 G. Lopez-Berestein, M. D. Landis, R. R. Rosato, B. Dave, S. Wong, D. Marchetti, A. K. Sood,
 J. C. Chang, HN1L promotes triple-negative breast cancer stem cells through LEPR-STAT3 pathway. Stem Cell Rep. 10, 212–227 (2018).
- J. Petroziello, A. Yamane, L. Westendorf, M. Thompson, C. McDonagh, C. Cerveny, C. L. Law, A. Wahl, P. Carter, Suppression subtractive hybridization and expression profiling identifies a unique set of genes overexpressed in non-small-cell lung cancer. *Oncogene* 23, 7734–7745 (2004).
- C. Grimm, K. Bartel, A. M. Vollmar, M. Biel, Endolysosomal cation channels and Cancer-A link with great potential. *Pharmaceuticals (Basel)* 11, 4 (2018).

- P. Faris, M. Shekha, D. Montagna, G. Guerra, F. Moccia, Endolysosomal Ca²⁺ signalling and cancer hallmarks: Two-pore channels on the move, TRPML1 lags behind! *Cancers* (*Basel*) 11, 27 (2018).
- G. P. Johnston, B. Bradel-Tretheway, P. D. Piehowski, H. M. Brewer, B. N. R. Lee, N. T. Usher, J. L. R. Zamora, V. Ortega, E. M. Contreras, J. R. Teuton, J. P. Wendler, K. M. Matz, J. N. Adkins, H. C. Aguilar, Nipah virus-like particle egress is modulated by cytoskeletal and vesicular trafficking pathways: A validated particle proteomics analysis. mSystems 4, e00194-19 (2019).
- B. Zybailov, A. L. Mosley, M. E. Sardiu, M. K. Coleman, L. Florens, M. P. Washburn, Statistical analysis of membrane proteome expression changes in *Saccharomyces cerevisiae*. J. Proteome Res. 5, 2339–2347 (2006).
- Y. Yang, L. Du, C. Liu, L. Wang, C. Ma, J. Tang, R. S. Baric, S. Jiang, F. Li, Receptor usage and cell entry of bat coronavirus HKU4 provide insight into bat-to-human transmission of MERS coronavirus. *Proc. Natl. Acad. Sci. U.S.A.* 111, 12516–12521 (2014).
- R. Aarhus, R. M. Graeff, D. M. Dickey, T. F. Walseth, H. C. Lee, ADP-ribosyl cyclase and CD38 catalyze the synthesis of a calcium-mobilizing metabolite from NADP. *J. Biol. Chem.* 270, 30327–30333 (1995).
- K. Ohgane, F. Karaki, K. Dodo, Y. Hashimoto, Discovery of oxysterol-derived pharmacological chaperones for NPC1: Implication for the existence of second sterol-binding site. *Chem. Biol.* 20, 391–402 (2013).
- M. Poštaa, V. Soósb, P. Beiera, Design of photoaffinity labeling probes derived from 3,4,5-trimethylfuran-2(5H)-one for mode of action elucidation. *Tetrahedron* 72, 3809–3817 (2016).
- C. J. Trabbic, F. Zhang, T. F. Walseth, J. T. Slama, Nicotinic acid adenine dinucleotide phosphate analogues substituted on the nicotinic acid and adenine ribosides. Effects on receptor mediated Ca²⁺ release. *J. Med. Chem.* 58, 3593–3610 (2015).

Acknowledgments: We would like to congratulate T.F.W. on his retirement and thank him for his support and encouragement of this project over the past decade. Funding: Work was supported by NIH GM088790 and NSF 2027748 (G.S.G., to J.S.M.), NIH R15-GM131329 (S.H., to J.T.S. and T.F.W.), and NIH P30 DA 013429 (E.B., to E.M.U.). S.P. was supported by BBSRC grants (BB/N01524X/1 and BB/T015853/1). Author contributions: G.S.G., T.F.W., E.B., and E.M.U. performed experiments or analyzed data. S.H. and J.T.S. performed chemical synthesis and validation. S.P. performed bioinformatic and phylogenetic analyses. G.S.G. directed the project with help from J.T.S., T.F.W., and J.S.M. G.S.G. and J.S.M. cowrote the manuscript with help from other authors. Competing interests: The authors declare that they have no competing interests. Data and materials availability: The MS proteomics data have been deposited to the ProteomeXchange Consortium via the PRIDE partner repository with the dataset identifier PXD024153 and 10.6019/PXD024153. All other data needed to evaluate the conclusions in this study are present within the paper or the Supplementary Materials.

Submitted 30 June 2020 Accepted 22 February 2021 Published 23 March 2021 10.1126/scisignal.abd5605

Citation: G. S. Gunaratne, E. Brailoiu, S. He, E. M. Unterwald, S. Patel, J. T. Slama, T. F. Walseth, J. S. Marchant, Essential requirement for JPT2 in NAADP-evoked Ca²⁺ signaling. *Sci. Signal.* **14**, eabd5605 (2021).

Science Signaling

Essential requirement for JPT2 in NAADP-evoked Ca²⁺ signaling

Gihan S. Gunaratne, Eugen Brailoiu, Shijun He, Ellen M. Unterwald, Sandip Patel, James T. Slama, Timothy F. Walseth and Jonathan S. Marchant

Sci. Signal. **14** (675), eabd5605. DOI: 10.1126/scisignal.abd5605

Connecting Ca2+ channels with NAADP

Connecting Ca2+ channels with NAADP

Although generation of the second messenger NAADP stimulates the release of Ca²⁺ from intracellular stores, binding sites for NAADP have not been characterized on NAADP-sensitive ion channels. Two papers independently identified an NAADP-binding protein called HN1L, which is also known as JPT2, that interacts with ryanodine receptors in the endoplasmic reticulum in T cells and two-pore channels (TPCs) in endosomes and lysosomes. Roggenkamp et al. found that HN1L deletion suppressed the formation of Ca²⁺ microdomains in stimulated Jurkat and primary rat T cells, one of the earliest responses to T cell receptor activation, thereby reducing global Ca²⁺ signaling. Gunaratne et al. found that knockdown of JPT2 attenuated NAADP-evoked Ca²⁺ signals from endosomes and lysosomes and the ability of a SARS-CoV-2 pseudocoronavirus to infect cells, a process that depends on TPC activity. Thus, HN1L/JPT2 enables NAADP to activate Ca²⁺ release from the endoplasmic reticulum through ryanodine receptors and from endosomes and lysosomes through TPCs lysosomes through TPCs.

ARTICLE TOOLS http://stke.sciencemag.org/content/14/675/eabd5605

SUPPLEMENTARY MATERIALS http://stke.sciencemag.org/content/suppl/2021/03/19/14.675.eabd5605.DC1

RELATED http://stke.sciencemag.org/content/sigtrans/14/675/eabh2798.full

http://stke.sciencemag.org/content/sigtrans/5/221/pe18.full http://stke.sciencemag.org/content/sigtrans/12/599/eaaz0961.full http://stke.sciencemag.org/content/sigtrans/11/561/eaat0358.full http://stke.sciencemag.org/content/sigtrans/14/675/eabd5647.full http://stke.sciencemag.org/content/sigtrans/14/675/eabd5647.full http://science.sciencemag.org/content/sci/365/6455/793.full

file:/content

REFERENCES This article cites 61 articles, 24 of which you can access for free

http://stke.sciencemag.org/content/14/675/eabd5605#BIBL

PERMISSIONS http://www.sciencemag.org/help/reprints-and-permissions

Use of this article is subject to the Terms of Service

Science Signaling (ISSN 1937-9145) is published by the American Association for the Advancement of Science, 1200 New York Avenue NW, Washington, DC 20005. The title Science Signaling is a registered trademark of AAAS.